Induced Flow and Coalescence Effects on Hydrogen Bubble Size Distribution Around a Single Wire Electrode in Alkaline Water Electrolysis.+

Pierre Van de Velde[1], Benoit Scheid[1], Joris Proost[b], Benoît Haut[1]

[a] *Université Libre de Bruxelles (ULB), TIPs, 50 Av Franklin Roosevelt, Brussels, 1050, , Belgium*
[b] *Université catholique de Louvain (UCL), Division of Materials and Process Engineering, Place Sainte-Barbe 2, Louvain-la-Neuve, 1348, , Belgium*

Abstract

In this study, we experimentally and theoretically examine the hydrogen bubble generation around a single horizontal wire electrode during alkaline water electrolysis. Wires form the elementary bricks of more complex mesh electrodes used in industrial systems. When detaching, the bubbles form a quasi 2D bubble curtain from which we measure the bubble size distributions at different current densities and electrolyte concentrations. Increasing the current density leads to larger and more disperse bubble sizes. This effect is stronger at low KOH concentrations for which we observe many coalescence events at the wire apex. We rationalize our observations by modeling the flow induced by the bubble curtain and using population balance equations to quantify how coalescence changes the bubble size distribution.

Keywords: bubbles, hydrogen, coalescence, flow, wire electrodes

1. Introduction

Driven by the growing demand for green hydrogen, several recent studies have focused on increasing the efficiency of electrolyzers. Several paths can be explored, including improvements in the electrode material, electrolyte concentration, operating conditions and, more recently, electrode geometry. In particular, mesh electrodes (Li et al. (2021)), metal foams (Rocha et al. (2022)) or even 3D printed structures (Rocha et al. (2023)) increase the contact area between the electrode and the solution, therefore also the amount of bubble nucleation sites. The main downside of these structures is the increased risk of bubbles remaining trapped in the electrode (Rocha et al. (2023)). The contribution of the bubbles to the overpotential has been studied extensively Yuan et al. (2023). While different strategies to remove them exist, we believe optimizing the electrode geometry can play a significant role in bubble management. As it is easier for small bubbles to escape pores than for large ones, it is capital to understand how the bubble size distribution is affected by the experimental conditions. When the water electrolysis reaction occurs, H_2 molecules are formed at the cathode and dissolved in the electrolyte, increasing the H_2 concentration close to the electrode. Once a critical supersaturation is reached, bubbles may nucleate on the electrode surface and grow until they reach their detachment radius. In general, bubbles detach once the buoyancy force overcomes the capillary force retaining the bubble on the electrode surface (Fritz (1935)). Nevertheless, other forces, such as electrostatic forces, or

fluid drag can also have significant effects (Van Helden et al. (1995); Yang et al. (2018)). Indeed, once detached, the bubbles rise and entrain some liquid leading to an induced flow at the scale of the electrolyzer. It has been shown that an increased flow implies a larger drag force, leading to the detachment of smaller bubbles (Duhar and Colin (2006)). Moreover, the flow may also lead to bubbles interacting with each other (Lubetkin (2002)). Upon contact, bubbles can coalesce, which drastically modifies the final bubble size distribution. Model experiments on the controlled coalescence of two bubbles have highlighted many parameters at play, such as the approach velocity, bubble volumes or the electrolyte concentration (Orvalho et al. (2015, 2021)). In general, when occurring between attached bubbles coalescence is beneficial for bubble detachment, as capillary energy is converted to kinematic energy promoting detachment. Overall, the size distribution depends a lot on the initial detachment radius of bubbles and their interactions, which are among many factors a consequence of the nucleation site distribution, current density and ion concentration. (Zhao et al. (2022); Zhang et al. (2024); Bashkatov et al. (2024)).

While several studies have focused on modeling the growth and detachment of single bubbles on micro-electrodes (Moreno Soto (2019); Bashkatov et al. (2019, 2022); Hossain et al. (2022)) or the size distribution of bubbles detaching from metal plates (Vogt (2017)), work on more complex structures remains to be done. On opaque porous electrodes such as metal foams or meshes, direct visualization of the bubbles is complex (Abdelghani-Idrissi et al. (2021)). Most studies hypothesize on the bubble size distribution around the electrodes and focus mainly on the electrochemical performance of the electrolyzer.

In this study, we propose to investigate the fundamental problem of the bubble behavior around and above a single horizontal wire electrode. Such a model electrode forms the elementary brick of more complex mesh electrodes and allows us to visualize bubble generation and coalescence events. This configuration is also of fundamental interest as it is found in various systems involving bubbles generated on wires. In particular, inspiration can be drawn from works on boiling liquids, which present many similarities with electrochemical systems (Park and Chung (2022)). By direct observation of the detached bubbles, we measure the bubble size distribution for a wide range of current densities and electrolyte concentrations. In particular, the KOH concentration influences the coalescence. Several studies show that for large enough pH, ions adsorb to the bubble surface, leading to electrostatic repulsion and reduced coalescence efficiency (Craig et al. (1993); Orvalho et al. (2015, 2021)). While both the mean bubble volume and the variance in bubble volumes increase with current density, we observe, at low KOH concentrations in the electrolyte, a stronger increase due to coalescence events at the wire apex, leading to a shift towards larger bubbles. To rationalize our observations, we model the induced flow with a single-phase approach that captures the flow field structure and velocities. We show how the flow structures favour coalescence and how this coalescence modifies the bubble size distributions. A model based on a population balance equation can reproduce the shift in mean bubble volume and variance in bubble sizes, due to coalescence events at the wire apex.

2. Materials and methods

2.1. Experimental setup

Figure 1 schematically presents the experimental setup used to study the bubble size distributions. A small 5x5x5 cm^3 plexiglass cuvette is filled with a KOH solution of known concentration c. A Nickel 201 mesh electrode serving as the anode and a Nickel 201 wire of known radius R serving as a cathode are immersed in the solution and connected to a laboratory power generator. The distance between the electrodes is kept constant between all experiments. The wire

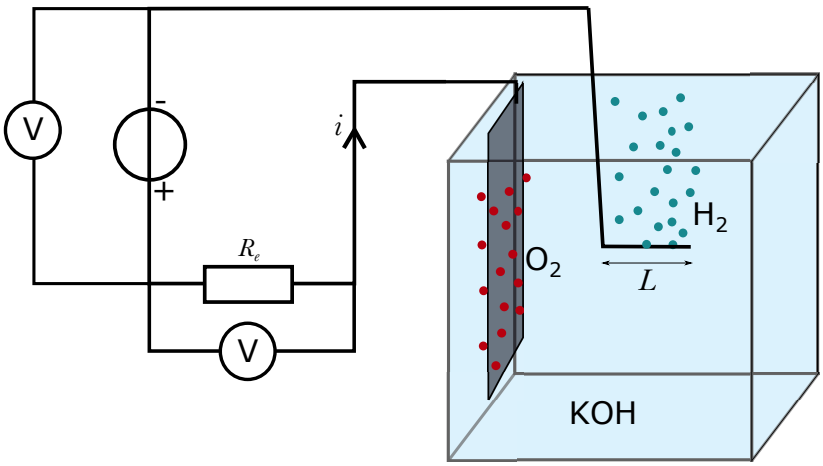

Figure 1: **Experimental setup.** A nickel mesh (anode) and a nickel wire of known radius R and length L (cathode) are immersed in a KOH solution contained in a 5x5x5 cm^3 plexiglass cuvette. A resistor $R_e = 100\ \Omega$ is placed in series with the electrolyzer and the current i is provided by a laboratory generator. The generator and the resistor are connected to two voltmeters (via a USB oscilloscope) to measure the tension and current applied to the electrodes.

electrode is oriented perpendicular to the mesh serving as the anode. The closest point of the wire is located 2 ± 0.2 cm away from the anode. The immersed portion of the anode is a 3x2 cm rectangle. We have not noticed any significant sensitivity of the electrical resistance to the slight changes in electrode positions in our system. However, it has been shown that with a smaller gap, the position of the electrodes influences the size of bubbles attached to wire electrodes (Rodriguez Osuna et al. (2022)). In our experiment a portion of length $L = 1$ cm of the wire is bent and maintained horizontally in the solution. The remaining (vertical) part of the wire is coated with a thin layer of PDMS to avoid any electrochemical reaction happening at its surface. The voltage and current are measured using a USB oscilloscope (Picoscope 2205A) measuring the potential difference between the two electrodes as well as on the two sides of a 100 Ω resistor placed in series with the cell.All experiments are performed at room temperature ($T = 293$K). Prior to any measurements, the electrodes are primed by operating them at a high voltage (15 V) for one hour. This procedure removes any dirt remaining from the wire fabrication process which could alter the wetting properties of the wire surface. After this treatment, the measured bubble size distributions are stable in time over the course of all our experiments. Moreover, this also allows the solution to be as close to saturation as possible before starting any measurement. In our experiments, we set the generator voltage to a constant value. After one minute of operation, both the cell voltage and the measured current remain constant over the course of one measurement. An LED light is placed behind the wire and pictures are taken using a digital camera (Ximea XiC) and a 60 mm lens.

2.2. Image analysis

Images of the wires and/or the bubbles detaching from the wire are analyzed using ImageJ and a custom Python code. The pictures obtained are first thresholded with an identical threshold value for all images. We use the *fill holes* and *watershed* functions to obtain full bubbles and to separate most bubble clusters. The built in function *analyze particles* then identifies groups of

connected pixels. The bubble radius is estimated from the measured bubble area. To avoid counting bubble clusters, we only count bubbles that have an eccentricity ($e = \sqrt{1 - b^2/a^2}$, where b and a are the major and minor axs of an ellipse fitted around the bubble edge) less than 0.05, giving us good confidence in our estimated radii. Moreover, we only consider bubbles that have a total area of at least 5 pixels (corresponding to $r = 5 \pm 1$ μm) to eliminate the noise.

3. Results

3.1. Phenomenological description

When water electrolysis occurs, H_2 molecules form at the wire (cathode) surface and dissolve in the electrolyte. Close to the wire, the H_2 concentration is thus higher than in the rest of the fluid. Once the hydrogen supersaturation is high enough (above the metastable zone) in the vicinity of the electrode, bubbles start to nucleate at the wire surface. Figure 2 shows typical images of hydrogen bubbles forming around and above a wire of radius $R = 250$ μm. We see that the amount of bubbles (figure 2A) or occupied nucleation sites (figure 2B) depends strongly on the imposed current density defined as

$$j = \frac{i}{2\pi RL}\,. \tag{1}$$

In fact, the gas flow rate is directly proportional to the current density, provided the liquid is saturated in dissolved gases. Consequently, at low current density (figures 2B(i-ii)), not all nucleation sites are occupied and most bubbles are smaller than 10 μm. When increasing the current density (see figures 2B(iii-v)), more nucleation sites become occupied. This increased density leads to some bubble-bubble interactions and coalescence events around and above the wire.

Figure 3 shows a perspective view of the horizontal wire (see also supplementary video 1). We can see the two types of bubbles formed at low current densities. Most bubbles are small compared to the wire radius when they detach. They follow the surface of the wire until they reach the wire apex. There, the bubble streams coming from both sides of the wire merge and the bubbles flow towards the surface forming a quasi-2D bubble curtain. The width of the curtain is defined by δ and is less than or equal to the wire diameter $\delta \lesssim 2R$. We expect the bubble curtain to induce a macroscopic flow in the cuvette, which in turn should affect the bubble sizes on the wire and in the bubble curtain as it influences the bubble detachment and possible coalescence events.

On the wire, some very large bubbles can also be observed (see video 1, figure 2B(i-iii) and figure 3). These bubbles are mainly located at the wire bottom and top and form on small defects on the wire surface (see section 6.2). Their exact detachment radius depends, among other parameters, on the induced flow, the local geometry of the wire surface and the electrolyte concentration. We will not attempt to predict their radius in this study. However, we have seen that the number of large bubbles (with a diameter $d > 0.3R$) decreases when the current increases. We assume that this is due to an increase in the induced flow velocity around the wire. The bubbles thus experience a stronger viscous drag, which leads to quicker detachment. The number of these very large bubbles being very small compared to the small bubbles, they have a very limited effect on the average bubble radii and size distributions. In all that follows, we focus primarily on the bubbles that are already detached and can be observed in the bubble curtain.

We want to understand how the bubble size distribution depends on the applied current density. To do this, we record videos of the bubble curtain. Since the curtain is thin enough, all bubbles

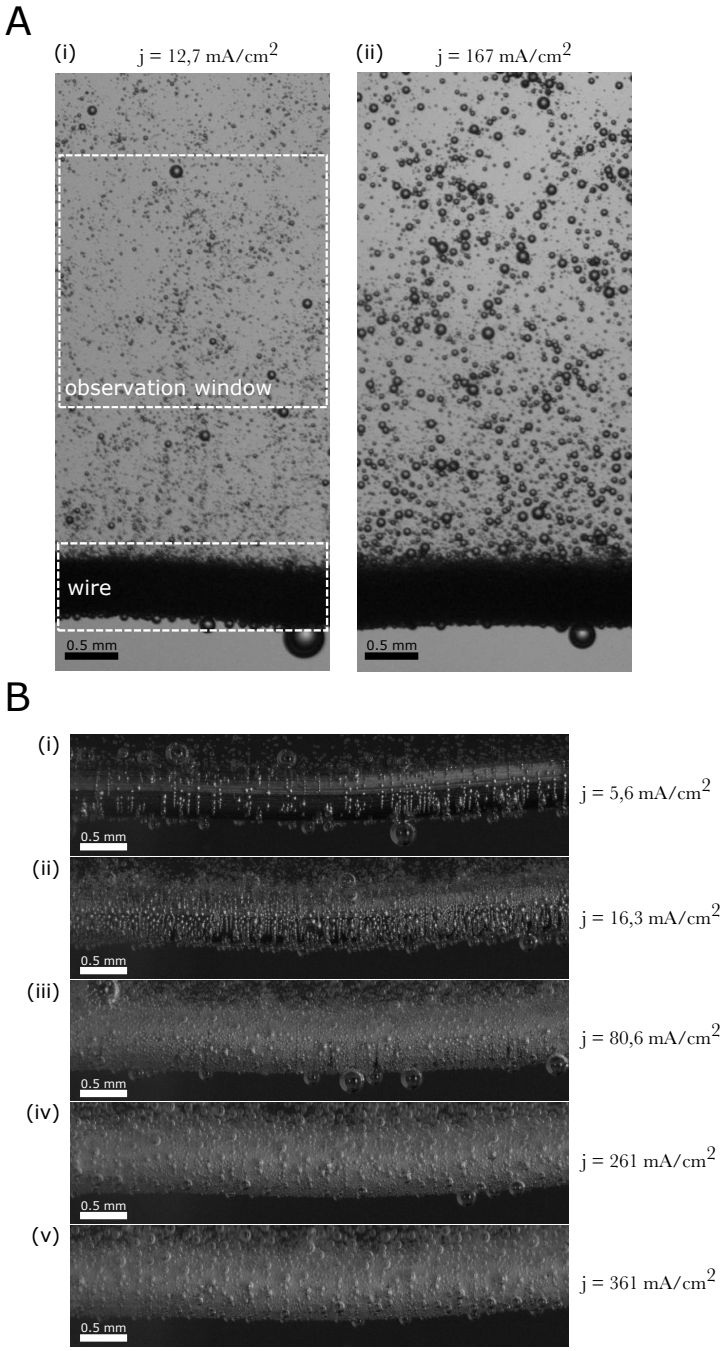

Figure 2: **Experimental pictures of hydrogen bubbles for different current densities.** **A** Front views of quasi-2D bubble curtain detaching from the wire, with the observation window used for subsequent analyses. **B** Close-up video snapshots of the wire for various current densities.

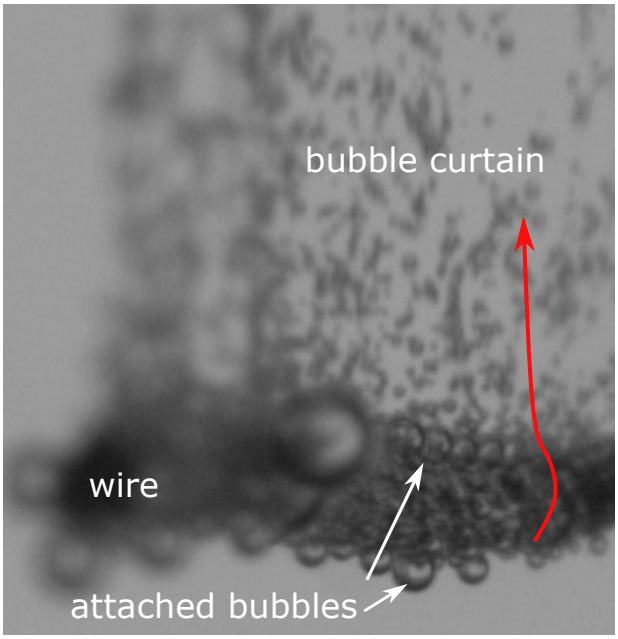

Figure 3: **Perspective view of the wire.** Image taken from supplementary video 1. Red arrow shows the typical path of a small bubble generated and detaching at the wire bottom. Larger bubbles remain attached mainly at the top or bottom of the wire.

remain in focus within the observation window shown in figure 2A(i). Within this window, no coalescence occurs. From figure 2A(i) we can see that, at a low current density (here $j = 12.7$ mA/cm^2), most bubbles are very small compared to the wire radius. The larger isolated bubbles that we observe are those that remained stuck on wire defects before detaching. At higher current densities, the bubbles are larger, as seen in figure 2A(ii). As the current density increases, the H_2 concentration close to the wire increases leading to faster bubble growth. The bubbles may also coalesce on the wire, increasing the overall bubble size. In addition to these phenomena, many coalescence events occur at the wire apex where the two bubble streams meet (see supplementary videos 2-6). These events further increase the size of the bubbles measured in the bubble curtain. In the following section, we characterize the bubble size distribution. The flow leading to these bubble streams is modeled and measured in section 4.1. In section 4.2 we then explain how this flow induces coalescence at the wire apex and how it affects the bubble size distribution.

3.2. Bubble size distributions

To quantitatively characterize the bubble size distribution, we analyze the images using ImageJ and a custom Python code. Distributions of the bubble radius r obtained for two different electrolyte concentrations are shown in figure 4A and B. They have been normalized by the total number of bubbles N_{tot} detected over one experiment, typically $N_{\text{tot}} \simeq 10^4$, measured within the observation window shown in figure 2A. Each curve is obtained from multiple images taken at a given current density, from 36 to 1785 mA.cm^{-2}. At low KOH concentration, the distribution is almost independent of the current densities below 200 mA.cm^{-2} in our experiments. Most

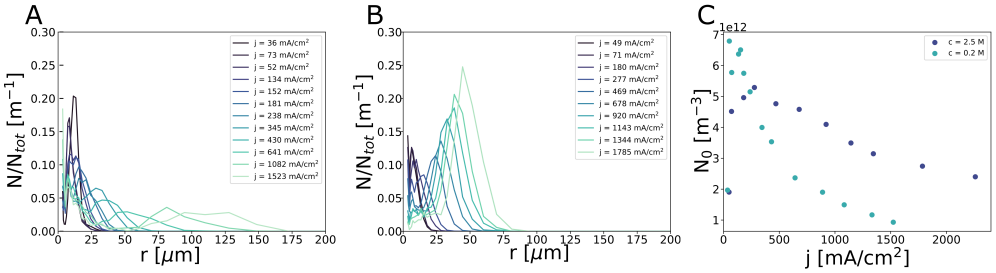

Figure 4: **Bubble size and density. A-B** Normalized distributions of bubble radius r for $c = 0.2$ M and 2.5 M KOH, respectively. **C** Bubble density N_0 in the bubble curtain for two KOH concentrations.

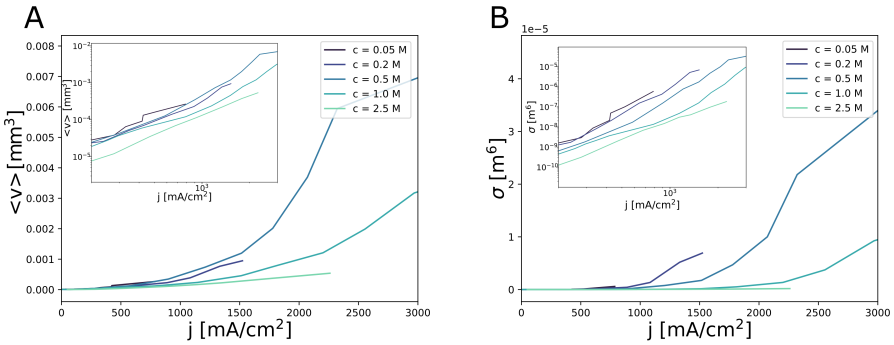

Figure 5: **Mean of the bubble size distribution and its variance. A** Mean bubble volume as a function of the current density measured for different concentrations ranging from 0.05 to 2.5 M. **B** Corresponding variance of the bubble volume. The insets show the same results in a log-log scale.

bubbles have a radius of about 25 μm and only a few larger bubbles are observed. Above a certain value of current (about 200 mA.cm^{-2} in this case), the size distribution is shifted toward larger bubbles. As mentioned previously, the mechanism behind this shift can be understood with the pictures of figure 2B and figure 3. At low current densities, the limiting factor seems to be the amount of occupied nucleation sites. Most bubbles detach at a small radius, forming two bubble streams that join the bubble curtain above the wire. Since the overall bubble density is low, almost no bubble coalescence is observed. When increasing the current density, all available nucleation sites at the wire surface are occupied by growing bubbles, forcing interactions between bubbles and thus coalescence. Moreover, we observe a lot of coalescence events at the apex of the wire, where the two bubble streams coming from each side of the wire merge. These coalescence events lead to a shift in the overall bubble size distribution.

This is confirmed by figure 4C, where we plot the bubble density $N_0 = N_{\text{tot}}/V_{\text{w}}$, with $V_{\text{w}} = 2RA_{\text{w}}$ the volume of the observation window, estimated by multiplying its surface A_{w} by the wire diameter $2R$. When increasing the current density, the bubble density first increases as more and more nucleation sites are occupied. After reaching a maximum around 100 mA.cm^{-2}, it decreases as more and more bubbles coalesce around the wire and at its apex forming larger bubbles. At higher ion concentrations, figure 4C shows that the decrease in the total number of bubbles is less pronounced because coalescence is inhibited by the electrostatic repulsion of adsorbed ions at the bubble surface (Craig et al. (1993); Orvalho et al. (2021)). This also leads to a different

bubble size distribution as shown in figure 4B. Indeed, for equivalent current densities, the bubble sizes are smaller and less spread out for large KOH concentrations.

Figure 5 summarizes these observations in terms of the mean volume of the bubble size distribution and its variance, calculated from the experimental data obtained for different KOH concentrations ranging from 0.05 to 2.5M. In figure 5A, we can see that the mean bubble volume is a nonlinear, increasing function of the current density. The higher the KOH concentration, the lower the mean volume. The same observations can be made for the variance shown in figure 5B. The reason for this difference is that less bubble coalescence is observed at high KOH concentrations.

We can conclude that the bubble size distribution is the result of many simultaneous phenomena. The flow field, which is induced by the bubbles themselves in the present configuration, has a strong influence as it affects detachment as well as coalescence between bubbles. A better understanding of the flow structures is thus needed to understand the size distributions. In the next section, we model and simulate the flow induced by the detached bubbles.

4. Modeling

4.1. Induced flow

We first aim to characterize the induced flow at the scale of the cuvette. The bubbles rising within the curtain cause a density gradient that induces a macroscopic flow in the cuvette. To explain this phenomenon we propose a single-phase approach that has been developed for a very similar (though larger scale) system, namely the induction of flow by a rising bubble curtain in caves (Martinelli et al. (2011)). We define the curtain as a region of width $\delta = 2R$ above the wire. In this region, the fluid has a lower density due to the presence of the bubbles. The gradient in buoyancy force then induces the flow. The main difficulty in this approach is to estimate the average density of the curtain implicitly linked to the amount of bubbles that it contains through the velocity of the induced flow.

The amount of gas that is produced can be estimated from the current going through the cell. Indeed, we can write the molar flux of H_2 molecules:

$$q_{\mathrm{H_2}} = \frac{q_{e^-}}{2} = \frac{i}{2F}\,, \tag{2}$$

where q_{e^-} is the molar electron flux and $F = 96500$ C.m^{-1} is the Faraday constant. We neglect the contribution of the capillary pressure in the bubbles here, since for bubbles with $r \geq 15\ \mu$m, it does not exceed 10% of the atmospheric pressure. The volumetric flux of gas generated at the cathode, using (2) and the ideal gas law, becomes

$$Q_{\mathrm{H_2}} = \frac{iR_gT}{2Fp}\,, \tag{3}$$

where p is the pressure, T is the temperature and R_g is the ideal gas constant. Integrating (3) over time gives the total amount of gas produced, which has been validated by comparison with experimental measurements, as shown in figure 10 of the appendix. The predicted values match the measured value, confirming the negligible contribution of the capillary pressure. We thus consider that all the produced hydrogen is captured in the bubbles over the course of our measurements. This is allowed by the fact that the solution is close to saturation when starting the measurements as explained in section 2.1.

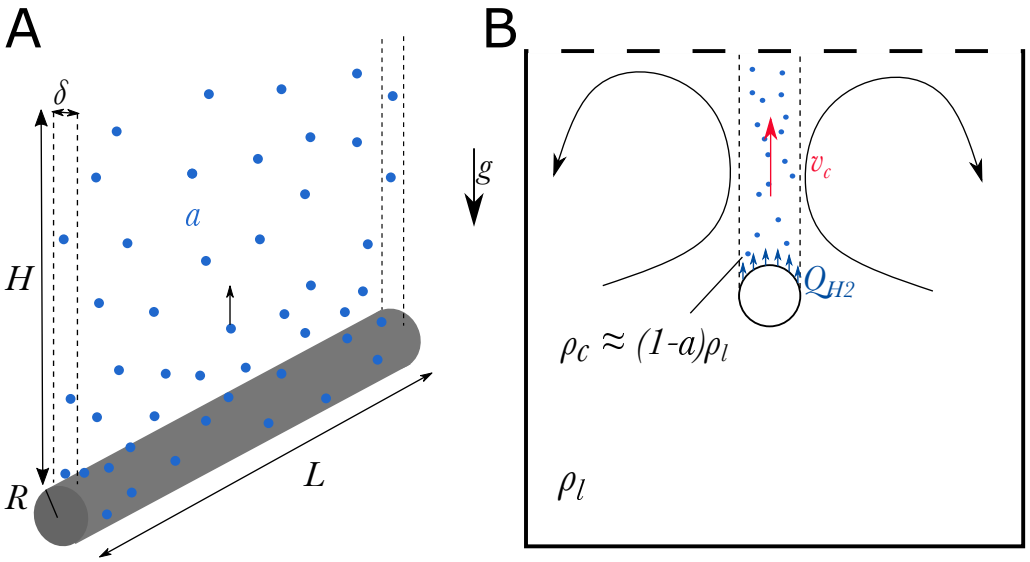

Figure 6: **Simulation domain A** Perspective sketch of the curtain of width $\delta = 2R$ and volumetric gas fraction α., the blue dots represent the bubbles.**B** Simulation domain depicting macroscopic recirculation induced by the incoming gas flux Q_{H_2} and the concomitant flow induced by the density contrast between the curtain and the bulk.

Experimentally, we observe that the bubbles rise at about 1 cm/s, from which we can calculate an order of magnitude of the Reynolds number of the bubbles, based on their diameter d. With a diameter of 30 μm, we obtain $\mathrm{Re} = v_b d/\nu_l \simeq 0.1$, where v_b is the absolute bubble velocity and ν_l the kinematic viscosity of the liquid. In our simulations, we assume that all bubbles have the same diameter and thus the same rising velocity. Throughout this section, we use $d = 30\,\mu$m for all simulations unless specified otherwise. This radius corresponds to the peak in bubble diameter we observe for for low currents. We will see later that the value of fluid velocity is relatively little sensitive to the choice of bubble diameter. We thus use the following formula to express the relative upward velocity of the bubbles, with respect to the fluid, obtained with a creeping flow approximation on a sphere with a stress-free interface (Ruiz-Rus et al. (2022)), namely

$$v_b^{\mathrm{rel}} = \frac{g\rho_l d^2}{12\mu}\,, \tag{4}$$

where g is the acceleration of gravity, μ is the dynamic viscosity of the liquid, and ρ_l is the liquid density. The absolute vertical velocity of the bubbles inside the curtain is thus

$$v_b = v_b^{\mathrm{rel}} + v_c\,, \tag{5}$$

where v_c is the average vertical velocity of the fluid within the curtain. The value of v_c depends on the average density of the fluid in the curtain, which can be written as

$$\rho_c = (1-\alpha)\rho_l + \alpha\rho_g \approx (1-\alpha)\rho_l\,, \tag{6}$$

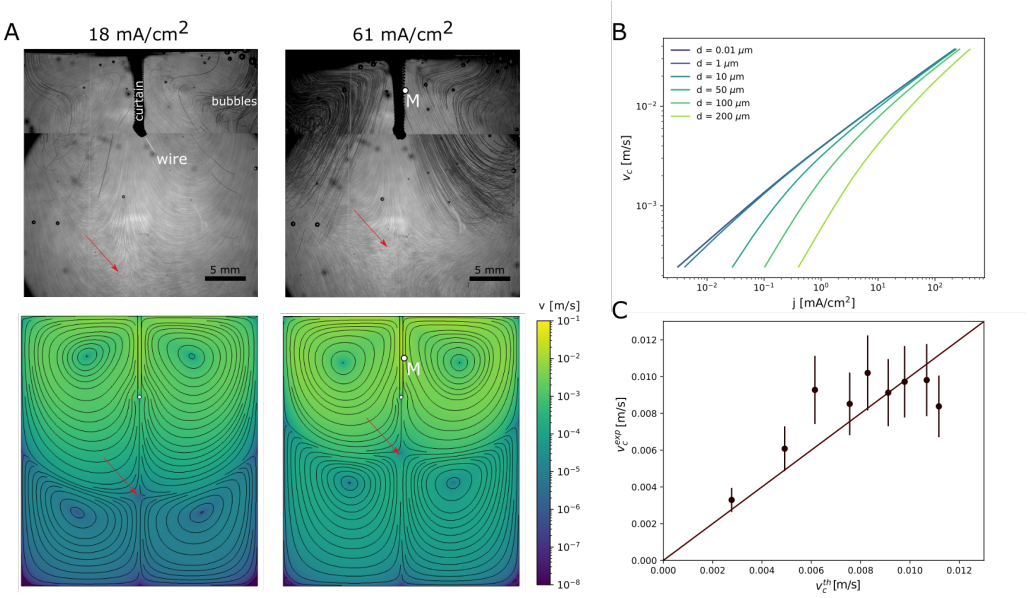

Figure 7: **Flow field around the wire. A:** Streamlines obtained experimentally (top row) and numerically (bottom row) for two different current densities. The wire is perpendicular to the plane. The curtain appears as a black line above the wire in the experimental pictures and is delimited by two vertical lines in the simulations. Note that the experimental views are reconstructed from two images obtained in the same conditions. The red arrows indicate the position of stagnation points. **B** Mean upward velocity of the fluid v_c in the bubble curtain as a function of the current density for different values of the bubble diameter d. **C** Comparison between experimental and theoretical values of the curtain velocity v_c measured at point M in panel A.

since the gas density $\rho_g \ll \rho_l$, and where α is the volume fraction of gas within the curtain. Knowing the gas flux coming from the wire, and using (4) and (5), we can estimate α as

$$\alpha \equiv \frac{V_{\text{air}}}{V_{\text{curtain}}} \approx \frac{Q_{\text{H}_2}}{\delta L(v_b^{\text{rel}} + v_c(\alpha))}\,, \tag{7}$$

where $V_{\text{air}} = Q_{\text{H}_2} H / v_b$ is the total volume of gaseous H_2 in the curtain and $V_{\text{curtain}} = \delta L H$ is the total volume of the curtain, with H the curtain height.

Assuming $\alpha \ll 1$ allows to write the continuity and Navier-Stokes equations within the Boussinesq approximation for a stationary regime,

$$\begin{cases} \nabla.\mathbf{u} = 0\,, \\ \rho_l(\mathbf{u}.\nabla)\mathbf{u} = -\nabla p + \rho\mathbf{g} + \mu\Delta\mathbf{u}\,, \end{cases} \tag{8}$$

with $\mathbf{u}$ the velocity field, and where $\rho = (1-\alpha)\rho_l$ in the curtain and $\rho = \rho_l$ outside the curtain, as illustrated in figure 6. The dynamic viscosity remains constant in the whole domain. Equations (8) are solved numerically using COMSOL Multiphysics with a no-slip boundary condition ($\mathbf{u} = 0$) on the wire surface, the lateral and bottom walls, and stress-free boundary condition on the top boundary ($\mathbf{u}_n = 0$, where $\mathbf{u}_n = 0$ is the normal velocity).

To find the link between current and gas volume fraction α, we solve (8) for many different values of α. This allows us to express the curtain velocity v_c as a function of α. The values of v_c

are shown in figure 12 in the appendix. Note that v_c is calculated as the average upward velocity of the fluid in the curtain calculated overe the entire curtain. Using the values of v_c for a given gas volume fraction α, we can solve for Q_{H_2} in (7), leading with (3) and (1) to the corresponding value of the current density.

Typical streamlines simulated for different values of current density are shown in the bottom row of figure 7A and compared in the upper row to experimental observations obtained by adding polystyrene tracer particles into the solution. Qualitatively, both the simulations and the experiments give very similar flow structures. At low values of α, the curtain induces two large convection cells having almost the dimensions of the tank on either side of the wire (not shown). When increasing the current density ($j = 18\,\mathrm{mA/cm^2}$), hence α, the overall fluid velocity becomes larger and two secondary cells appear at the bottom of the tank. The stagnation point shown by the red arrow rises as the cells grow with increasing the current density and reach almost half the size of the overall tank for the large value ($j = 61\,\mathrm{mA/cm^2}$).

Figure 7B shows the computed curtain velocity for different values of current density and bubble diameter. As expected, the velocity increases with increasing the current density, or equivalently increasing the gas volume fraction. Moreover, and especially for small gas volume fractions, the variation in v_c can be as much as two orders of magnitude depending on the bubble diameter. Larger bubbles lead to a smaller fluid flow. Indeed, as the relative velocity (4) of bubbles increases with their diameter, it reduces the curtain velocity for a given α, as it can be inferred from (7). Physically, it means that larger bubbles have shorter residence times, leading to a lower gas volume fraction within the curtain. We also see that the relative influence of the bubble size through v_b^{rel} decreases with increasing current. The choice of a constant d, considering the sensitivity of v_c to this parameter, is a potential source of error in our model. However, within the range of current densities in our experiments, the largest relative difference in v_c between simulations made with $d = 1$ μm and $d = 200$ μm is 16 %. We thus consider that taking a constant value of d is satisfactory to estimate the fluid velocity in the curtain.

In figure 7C, we compare the curtain velocity at point M, taken halfway between the wire apex and the upper interface on one side of the curtain, as predicted by the model, v_c^{th}, and measured with the velocity of the tracer particles, v_c^{exp}. Since, in the experiments, the curtain is a discontinuous two-phase mixture, the velocity of a tracer particle coming close to point M depends a lot on the local presence or not of a bubble at that point. Moreover, the trajectory of a tracer particle does not always follow the curtain perfectly, hence the large error bars. Nonetheless, from figure 7C, we see that we have a good agreement between the model and the experiments for low values of current density. At higher current density, hence higher gas fraction, the measured experimental velocity seems to plateau at around 1 cm/s. There are several possible explanations for this plateau, such as the dependence of v_c to the bubble diameter, bubbles that are re-injected from the fluid surface into the convection cells or 3D effects that are not captured by the model. Yet, this effect is only limited to high current density and our results confirm that the model properly captures the main flow structures and satisfactorily predicts the curtain velocity.

We now aim to explain how these flow structures influence the bubble size distribution through favoring bubble coalescence at the wire apex. Figure 9A shows the predicted velocity vectors close to the wire. The direction of these vectors is the same for all examined flow rates, with a stagnation point at the wire apex. This explains why the bubble streams forming on either side of the wire meet at the apex. At that position, a lot of bubbles come into contact, thus favoring coalescence. In the next section, we construct a model based on this flow structure and a population balance equation to explain the shift in bubble sizes described in section 3.2.

4.2. *Coalescence at the wire apex*

4.2.1. *Population balance equation*

In this section, we aim to explain the observed shift in the bubble size distributions reported in section 3.2. We describe the process using population balance equations which are commonly used to describe particle, droplet or bubble sizes in different contexts (Scott (1968); Bryson and Hofman (1989); Coufort et al. (2007); Ruiz-Rus et al. (2022)).

As shown in figure 9, we define a small region of volume V, located at the wire apex. Two

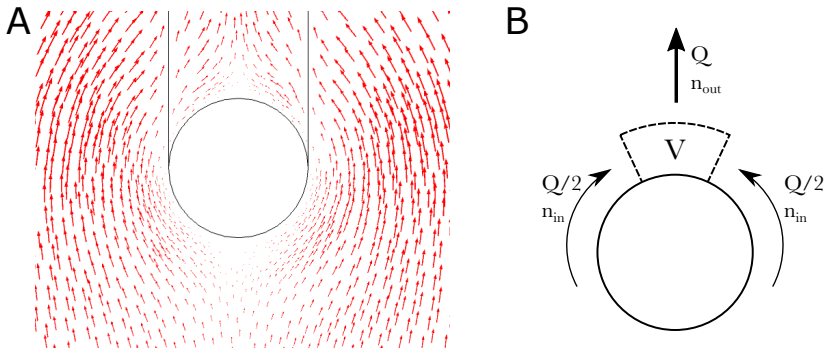

Figure 8: **Modeling principle. A** Velocity vectors around the wire for $\alpha = 0.03$ obtained using COMSOL. **B** Notations used to write the population balance equations.

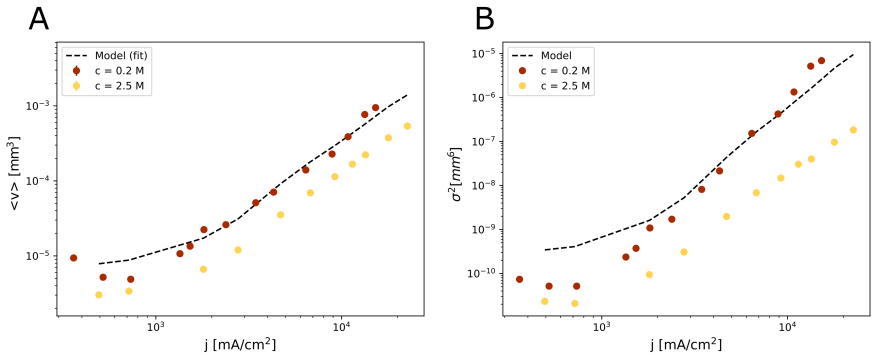

Figure 9: **Effect of coalescence. A** Average bubble volume in the stream leaving the volume V for different current values and different KOH concentrations. At high currents, coalescence increases the spread in bubble volumes, especially for low concentrations. The black line is obtained by fitting the value of q^* in equation 25. **B** Measured variance of the bubble volume in the outcoming stream for two different concentrations. The black dotted line is the variance predicted by the model.

bubble streams, mixtures of bubbles and liquid, each with a fluid flow rate $Q/2$, coming from both sides of the wire enter this region while a single stream of flux Q comes out of it. The incoming size distribution of the bubbles in the streams entering the volume V is noted $n_{\text{in}}(v,t)$, and expressed in m^{-6}, as it is defined per unit volume of fluid, with v the bubble volume and t the time. This incoming distribution generated at the wire depends on the roughness, the current and the surrounding flow, and is *a priori* unknown. The outcoming distribution $n_{\text{out}}(v,t)$ depends on

n_{in} and on the coalescence events. Assuming that the volume V is perfectly mixed, the classical population balance equation (Ruiz-Rus et al. (2022)) writes

$$V\frac{\partial n_{\text{out}}(v,t)}{\partial t} = Q\left(n_{\text{in}}(v,t) - n_{\text{out}}(v,t)\right) + V\frac{1}{2}\int_0^v q(u, v-u)n_{\text{out}}(u,t)n_{\text{out}}(v-u,t)\mathrm{d}u - V\int_0^\infty q(u,v)n_{\text{out}}(u,t)n_{\text{out}}(v,t)\mathrm{d}u\,, \quad (9)$$

where u is a dummy variable, having the dimension of a volume, for integration. The two integral terms account for bubbles created and removed by coalescence events respectively; q is called the coalescence kernel and is the product of a collision frequency, *i.e.* how often particles come into contact, and a coalescence efficiency, *i.e.* the probability that an interaction leads to coalescence (Ruiz-Rus et al. (2022)). In principle, q thus depends on the relative velocity of two bubbles, hence on the flow, as well as on the bubble sizes. In all that follows, we assume that q is independent of the bubble sizes, which is the simplest possible choice of coalescence kernel. Other choices accounting for the bubble sizes are possible (Scott (1968)).
We define the following dimensionless quantities,

$$\tilde{t} = \frac{t}{V/Q}\,, \quad (10)$$

$$\tilde{v} = \frac{v}{v_{\text{ref}}}\,, \quad (11)$$

$$\tilde{u} = \frac{u}{v_{\text{ref}}}\,, \quad (12)$$

where v_{ref} is a reference bubble volume. We also define dimensionless distributions as

$$\tilde{n}_a(\tilde{v}) = \frac{n_a(\tilde{v}v_{\text{ref}})}{N_{\text{ref}}}v_{\text{ref}}\,, \quad (13)$$

with $a = \{\text{in,out}\}$ and N_{ref} a typical number density. We then non-dimensionalize (9) to obtain, in the stationary regime,

$$0 = \tilde{n}_{\text{in}}(\tilde{v}) - \tilde{n}_{\text{out}}(\tilde{v}) + \frac{1}{2}\int_0^{\tilde{v}} \tilde{q}(\tilde{u}, \tilde{v}-\tilde{u})\tilde{n}_{\text{out}}(\tilde{u})\tilde{n}_{\text{out}}(\tilde{v}-\tilde{u})\mathrm{d}\tilde{u} - \int_0^\infty \tilde{q}(\tilde{u},\tilde{v})\tilde{n}_{\text{out}}(\tilde{u})\tilde{n}_{\text{out}}(\tilde{v})\mathrm{d}\tilde{u}\,, \quad (14)$$

with $\tilde{q} = \dfrac{qN_{\text{ref}}}{Q/V}$ a dimensionless kernel that is independent of $\tilde{u}$ and $\tilde{v}$. Knowing n_{in}, it is thus possible to solve for n_{out} numerically (Kumar and Ramkrishna (1996)), for a given value of $\tilde{q}$.

4.2.2. Mean bubble volume and variance

To go further analytically, we consider the first three moments of the distribution. The i-th moment of a distribution is defined as

$$\tilde{\mu}_i = \int_0^\infty \tilde{v}^i\tilde{n}(\tilde{v})\mathrm{d}\tilde{v}\,. \quad (15)$$

By going back to the dimensional quantities we get

$$\tilde{\mu}_i = \frac{1}{N_{\text{ref}} v_{\text{ref}}^i} \int_0^\infty v^i n(v) \mathrm{d}v. \tag{16}$$

We write $N = \int_0^\infty n(v)\mathrm{d}v$ the 0-th moment of any distribution. It is the amount of bubbles per unit volume of the bubble-liquid mixture. The mean volume of the distribution is given by

$$\langle v \rangle = \frac{\int_0^\infty v n(v) \mathrm{d}v}{N} \ , \tag{17}$$

and the variance of the distribution is defined as

$$(\sigma)^2 = \frac{\int_0^\infty (v - \langle v \rangle)^2 n(v) \mathrm{d}v}{N} \, . \tag{18}$$

Manipulating the previous equations, we get the following expressions for the first three moments of $\tilde{n}_{\text{in}}$ and $\tilde{n}_{\text{out}}$,

$$\begin{cases} \tilde{\mu}_0^a = \dfrac{N^a}{N_{\text{ref}}} \\ \tilde{\mu}_1^a = \dfrac{N^a \langle v \rangle^a}{N_{\text{ref}} v_{\text{ref}}} \\ \tilde{\mu}_2^a = \dfrac{(\sigma^a)^2 + (\langle v \rangle^a)^2}{\frac{N_{\text{ref}}}{N^a} v_{\text{ref}}^2} \end{cases} , \tag{19}$$

with a = in or out. By further defining $\tilde{N} = \dfrac{N}{N_{\text{ref}}}$, $\langle \tilde{v} \rangle = \dfrac{\langle v \rangle}{v_{\text{ref}}}$ and $\tilde{\sigma} = \dfrac{\sigma}{v_{\text{ref}}}$, we can simplify the above expressions to

$$\begin{cases} \tilde{\mu}_0^a = \tilde{N}^a \\ \tilde{\mu}_1^a = \tilde{N}^a \langle \tilde{v} \rangle^a \\ \tilde{\mu}_2^a = \tilde{N}^a \left[(\tilde{\sigma}^a)^2 + (\langle \tilde{v} \rangle^a)^2 \right] \end{cases} . \tag{20}$$

We now aim to find links between the moments of n_{in} and n_{out}. To do so, we multiply (14) by v^i, with $i = \{1,2,3\}$, and integrate, which leads to

$$\begin{cases} \tilde{\mu}_0^{\text{in}} - \tilde{\mu}_0^{\text{out}} - \dfrac{\tilde{q}}{2} (\tilde{\mu}_0^{\text{out}})^2 = 0 \\ \tilde{\mu}_1^{\text{in}} = \tilde{\mu}_1^{\text{out}} \\ \tilde{\mu}_2^{\text{in}} - \tilde{\mu}_2^{\text{out}} + \tilde{q} (\tilde{\mu}_1^{\text{out}})^2 = 0 \end{cases} . \tag{21}$$

see **??** for more details. Combining the above equations and defining $q^* = \tilde{q} \tilde{N}^{\text{in}}$, we finally obtain

$$\begin{cases} \langle \tilde{v} \rangle^{\text{out}} = \langle \tilde{v} \rangle^{\text{in}} \dfrac{q^*}{\sqrt{1 + 2q^*} - 1} \\ (\tilde{\sigma}^{\text{out}})^2 = \dfrac{1}{2} \left[(\tilde{\sigma}^{\text{in}})^2 \left(1 + \sqrt{1 + 2q^*} \right) + q^* \sqrt{1 + 2q^*} (\langle \tilde{v} \rangle^{\text{in}})^2 \right] \end{cases} . \tag{22}$$

Equations (22) thus give us the evolution of the average volume and the variance due to coalescence. We can calculate simplified expressions at leading order in q^*:
For $q^* \ll 1$, *i.e.* for low coalescence efficiency, we obtain

$$\langle \tilde{v} \rangle^{\text{out}} = \langle \tilde{v} \rangle^{\text{in}} \, , \tag{23}$$

Panel (appendix)	radius [μm]	concentration [mol.L^{-1}]	q* [\]
A	150	0.20	12.5
B	150	0.20	12.5
C	250	0.20	18.0
D	150	0.05	20.4
E	150	0.50	19.2

Table 1: **Estimated values of q^*** obtained as a best fit from the data presented in figure 13 in the appendix. Panels A and B were obtained with the same configuration but with two distinct but identical wires.

and

$$(\tilde{\sigma}^{\text{out}})^2 = (\tilde{\sigma}^{\text{in}})^2 + \frac{q^*}{2}\left((\tilde{\sigma}^{\text{in}})^2 + (\langle\tilde{v}\rangle^{\text{in}})^2\right). \tag{24}$$

For $q^* \gg 1$, *i.e.* for large coalescence efficiency, we obtain

$$\langle\tilde{v}\rangle^{\text{out}} = \sqrt{\frac{q^*}{2}}\langle\tilde{v}\rangle^{\text{in}}, \tag{25}$$

and

$$(\tilde{\sigma}^{\text{out}})^2 = \sqrt{\frac{q^*}{2}}\left[(\tilde{\sigma}^{\text{in}})^2 + q^*(\langle\tilde{v}\rangle^{\text{in}})^2\right]. \tag{26}$$

4.2.3. Experimental validation

We now compare the description of section 4.2 to our experimental size distributions. The main challenge is that measuring n_{in} is difficult because the bubbles moving along the wire do not stay in the same plane and reflections from the wire surface limit the contrast. However, we have described that coalescence is inhibited at high KOH concentrations. In this case, q^* tends to 0 and $n_{in} = n_{out}$ which is consistent with (14). We thus decide to use the distribution in the curtain n_{out} observed at the highest KOH concentration, *i.e.* $c = 2.5$ M, as an input distribution n_{in} for the lower concentrations. In other words, we take the values of $\langle v\rangle^{\text{out}}$ and $(\sigma^{\text{out}})^2$ obtained at the highest concentration as $\langle v\rangle^{\text{in}}$ and $(\sigma^{\text{in}})^2$ for all other concentrations. In figure 9A, we plot the values of $\langle v\rangle$ for two extreme concentrations $c = 0.2$ and 2.5 M. We see that, at high current density, $\langle v\rangle^{\text{out}}_{\text{c=0.2M}}$ is proportional to $\langle v\rangle^{\text{out}}_{\text{c=2.5M}}$ which we suppose equal to $\langle v\rangle^{\text{in}}_{\text{c=0.2M}}$. Thus, (25) seems valid which indicates that $q^* \gg 1$ at high current density. From the data, we can thus estimate $q^* = 12.5$ using (25). The black dotted line in figure 9 shows the values obtained by fitting the value of q^* in (25). Finally, using (26), we can calculate $(\sigma^{\text{out}}_{\text{c=0.2M}})^2$ from $(\sigma^{\text{in}}_{\text{c=0.2M}})^2 = (\sigma^{\text{out}}_{\text{c=2.5M}})^2$ and $\langle v\rangle^{\text{in}}_{\text{c=0.2M}} = \langle v\rangle^{\text{out}}_{\text{c=2.5M}}$. We obtain the dotted line shown in figure 9B, which gives an accurate prediction of $(\sigma^{\text{out}})^2$. This procedure works for different wire radii and ion concentrations we tried (see figure 13 in the appendix). Although we cannot predict the size distribution, our model captures the effect of coalescence at the wire apex by rationalizing the shift in size distribution between n_{in} and n_{out}. Given the significant approximations made, such as the choice of a kernel independent of the bubble size, the good agreement confirms the correct description of the coalescence process. Table 1 shows the values of q^* estimated using (25) for different parameters. From this data it seems that a larger wire radius and smaller concentrations lead to larger values of q^* i.e. a larger coalescence efficiency.

5. Discussion and conclusion

In this work, we have described the bubble size distribution around a model wire electrode. This model system allows an easy visualization of the detached bubbles which allows to test the effect of different parameters, such as the electrolyte concentration or current density on the bubble size distribution. The mean bubble size and its variance increase with increasing current density. However, this increase is even more significant at low KOH concentrations, where coalescence events occur at the wire apex. The detached bubbles form a quasi-2D curtain above the wire, inducing convection cells in the fluid at the scale of the cuvette. We modeled this induced flow using a single phase approach which proved to be in good agreement with the experimental data. Around the wire, two bubble streams, driven by this induced flow, meet at the wire apex leading to coalescence. The effect of coalescence on the size distribution is captured by a population balance equation with a constant coalescence kernel. Despite the apparent simplicity of this model setup, we see that many different problems involving hydrodynamics, electrochemistry and bubble mechanics are coupled. We believe that this experiment allows us to understand and model the different phenomena at play in more complex systems. In the zero-gap configuration used in most applications a big portion of the wire is in contact with the membrane separating anode and cathode. The effect of the membrane on the flow could be introduced in our simulations by adding some obstacles.

Several aspects of this work could be enhanced to further understand the behaviour of bubbles around electrodes. While the single-phase approach is already powerful to model the flow induced by the bubbles, a proper multi-phase model would be useful in particular for more complex geometries. Moreover, 3D simulations could maybe capture more detailed flow structures around the electrodes. We have shown that the flow patterns, and in particular the presence of a stagnation point at the wire apex, induce coalescence events shifting the bubble size distributions towards larger size. Such simulations could thus be useful to develop electrode shapes minimizing coalescence and thus favoring the evacuation of detached bubbles (Rocha et al. (2023)).

Our coalescence model also has its limitations. In particular, the choice of a constant coalescence kernel could be discussed. Other more complex choices in which the coalescence efficiency depends on the bubble size or velocity could be made. Although all experiments were performed at room temperature, the temperature change caused by the heating of the wire may also modify the bubble kernel Ribeiro and Mewes (2006). Moreover, the present model could be extended to consider coalescence directly on the wire. This could explain the increase in bubble size observed as the current increases for all concentrations.

6. Appendix

6.1. Validation of equation 3

To validate equation 3, water electrolysis was performed for several hours, collecting the produced hydrogen in an inverted falcon tube placed above the wire. The tube being initially filled with electrolyte, this method allows for a direct measurement of the total volume of the bubbles. Figure 10 compares the measured volume to the volume estimated by integrating equation 3 over the course of the experiment. The measured and estimated volumes are very close. We can thus use the current measurement as a direct measure of the produced hydrogen.

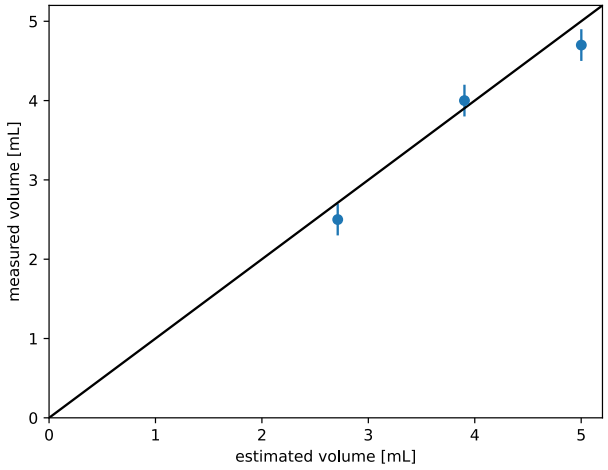

Figure 10: **Estimated vs measured volume**. Experimentally measured volume for three different experiments (different current densities and duration) compared to the volume estimated by integrating (3).

6.2. Wire surface structure

The presence of very large bubbles ($d > 200\ \mu$m) can be attributed to the surface structure of the electrodes. Figure 11 shows a picture of the wire surface observed under a microscope. We can clearly see groves at the wire surface in the direction of the wire. We also observe some local more circular defects. These groves and defects are a result of the drawing process and can serve as pinning points for the largest bubbles.

6.3. Curtain velocity

Figure 12 shows the average upward velocity in the curtain for different gas fractions α in the curtain obtained from our simulations. By definition of α, the value does not depend on the bubble diameter.

6.4. Finding the relationships between the moments of the distribution.

In this section, we detail the calculations to get from equation 14 to equations 21. For simplicity, we will drop the tilde on u and v. We first multiply equation 14 by v^i (with i an integer) and integrate for v from 0 to ∞, which writes, for a constant value of q :

$$0 = \int_0^\infty v^i n_{\text{in}}(v)\mathrm{d}v - \int_0^\infty v^i n_{\text{out}}(v)\mathrm{d}v + \frac{q}{2}\int_{v=0}^\infty \int_{u=0}^v v^i n_{\text{out}}(u) n_{\text{out}}(v-u)\mathrm{d}u\mathrm{d}v - q\int_0^\infty \int_0^\infty v^i n_{\text{out}}(u) n_{\text{out}}(v)\mathrm{d}u\ . \quad (27)$$

We perform the following change of variables in the first double integral : $x = u$, $y = v - u$. In the (u,v) space, the integration domain is a triangle which is limited by the lines $u = 0$, $v = 0$ and

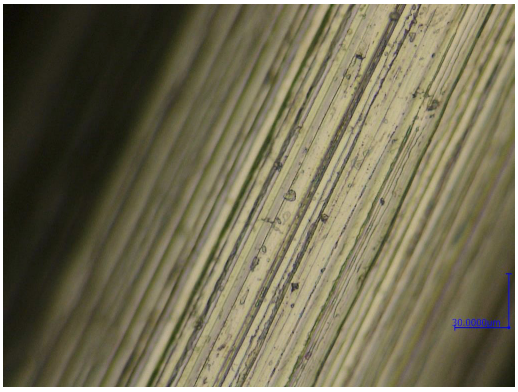

Figure 11: **Surface of the wire** observed under a microscope (50x).

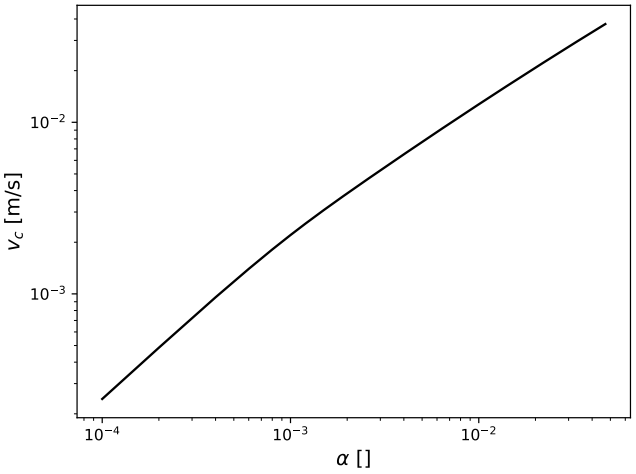

Figure 12: **Curtain velocity** as a function of the gas volume fraction.

$u = v$ which corresponds to the half space limited by the lines $x = 0$ and $y = 0$. After this change of variables, we can thus rewrite the previous equation:

$$0 = \int_0^\infty v^i n_{\text{in}}(v)\mathrm{d}v - \int_0^\infty v^i n_{\text{out}}(v)\mathrm{d}v + \frac{q}{2}\int_{x=0}^\infty \int_{y=0}^\infty v^i n_{\text{out}}(x) n_{\text{out}}(y)\mathrm{d}x\mathrm{d}y - q\int_0^\infty \int_0^\infty v^i n_{\text{out}}(u) n_{\text{out}}(v)\mathrm{d}u\mathrm{d}v\,, \quad (28)$$

which simplifies to the following :

$$0 = \int_0^\infty v^i n_{\text{in}}(v)\mathrm{d}v - \int_0^\infty v^i n_{\text{out}}(v)\mathrm{d}v - \frac{q}{2}\int_0^\infty \int_0^\infty v^i n_{\text{out}}(u) n_{\text{out}}(v)\mathrm{d}u\mathrm{d}v\,, \quad (29)$$

from which we can get equations 21 by integrating for i = 0, 1 and 2 successively.

6.5. Validation of the coalescence model

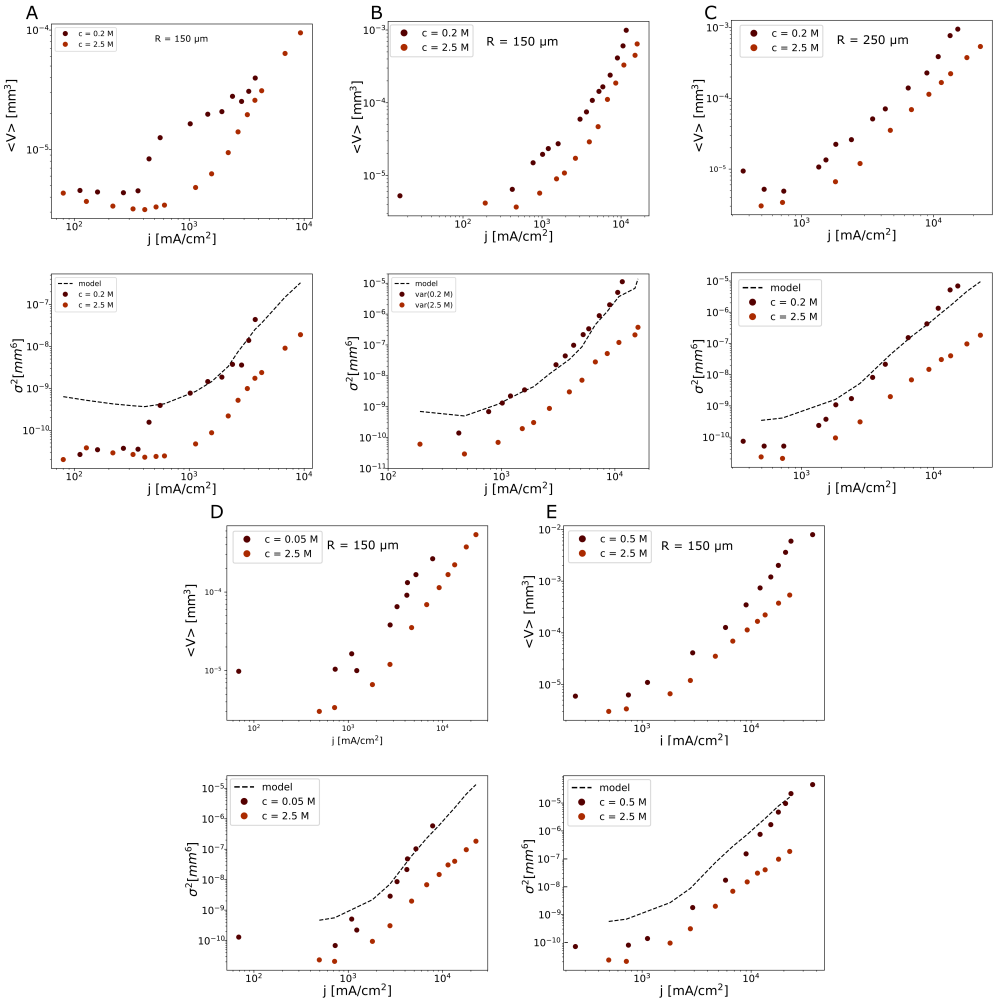

Figure 13: **Coalescence model validation.** Mean volume and variance for different wire radii and electrolyte concentrations. The dotted line corresponds to the prediction of (26), using the data at high KOH concentration for $\langle \nu \rangle$ and σ^2.

Figure 13 shows the mean volumes and variances calculated for five different sets of parameters. As in figure 9 we obtain the estimation of the coalescence at low concentration from the data obtained at high KOH concentration. The values of q^* used in the model are shown in table 1.

References

Abdelghani-Idrissi, S., Dubouis, N., Grimaud, A., Stevens, P., Toussaint, G., Colin, A., 2021. Effect of electrolyte flow on a gas evolution electrode. Scientific Reports 11, 4677. URL: https://www.nature.com/articles/s41598-021-84084-1, doi:10.1038/s41598-021-84084-1.

Bashkatov, A., Hossain, S.S., Mutschke, G., Yang, X., Rox, H., Weidinger, I.M., Eckert, K., 2022. On the growth regimes of hydrogen bubbles at microelectrodes. Physical Chemistry Chemical Physics 24, 26738–26752. URL: http://xlink.rsc.org/?DOI=D2CP02092K, doi:10.1039/D2CP02092K.

Bashkatov, A., Hossain, S.S., Yang, X., Mutschke, G., Eckert, K., 2019. Oscillating Hydrogen Bubbles at Pt Microelectrodes. Physical Review Letters 123, 214503. URL: https://link.aps.org/doi/10.1103/PhysRevLett.123.214503, doi:10.1103/PhysRevLett.123.214503.

Bashkatov, A., Park, S., Demirkır, , Wood, J.A., Koper, M.T.M., Lohse, D., Krug, D., 2024. Performance Enhancement of Electrocatalytic Hydrogen Evolution through Coalescence-Induced Bubble Dynamics. Journal of the American Chemical Society 146, 10177–10186. URL: https://pubs.acs.org/doi/10.1021/jacs.4c02018, doi:10.1021/jacs.4c02018.

Bryson, A.W., Hofman, D.L., 1989. A population balance approach to the study of bubble behaviour at gas-evolving electrodes. Journal of Applied Electrochemistry 19, 116–119. URL: http://link.springer.com/10.1007/BF01039401, doi:10.1007/BF01039401.

Coufort, C., Bouyer, D., Liné, A., Haut, B., 2007. Modelling of flocculation using a population balance equation. Chemical Engineering and Processing: Process Intensification 46, 1264–1273. URL: https://linkinghub.elsevier.com/retrieve/pii/S0255270106002558, doi:10.1016/j.cep.2006.10.012.

Craig, V.S.J., Ninham, B.W., Pashley, R.M., 1993. The effect of electrolytes on bubble coalescence in water. The Journal of Physical Chemistry 97, 10192–10197. URL: https://pubs.acs.org/doi/abs/10.1021/j100141a047, doi:10.1021/j100141a047.

Duhar, G., Colin, C., 2006. Dynamics of bubble growth and detachment in a viscous shear flow. Physics of Fluids 18, 077101. URL: http://aip.scitation.org/doi/10.1063/1.2213638, doi:10.1063/1.2213638.

Fritz, W., 1935. Berechnung des maximalvolumes von dampfblasen. Physik. Zeitschr , 379–384.

Hossain, S.S., Bashkatov, A., Yang, X., Mutschke, G., Eckert, K., 2022. Force balance of hydrogen bubbles growing and oscillating on a microelectrode. Physical Review E 106, 035105. URL: https://link.aps.org/doi/10.1103/PhysRevE.106.035105, doi:10.1103/PhysRevE.106.035105.

Kumar, S., Ramkrishna, D., 1996. On the solution of population balance equations by discretization—I. A fixed pivot technique. Chemical Engineering Science 51, 1311–1332. URL: https://linkinghub.elsevier.com/retrieve/pii/0009250996884892, doi:10.1016/0009-2509(96)88489-2.

Li, L., Jiang, W., Zhang, G., Feng, D., Zhang, C., Yao, W., Wang, Z., 2021. Efficient Mesh Interface Engineering: Insights from Bubble Dynamics in Electrocatalysis. ACS Applied Materials & Interfaces 13, 45346–45354. URL: https://pubs.acs.org/doi/10.1021/acsami.1c07637, doi:10.1021/acsami.1c07637.

Lubetkin, S., 2002. The motion of electrolytic gas bubbles near electrodes. Electrochimica Acta 48, 357–375. URL: https://linkinghub.elsevier.com/retrieve/pii/S0013468602006825, doi:10.1016/S0013-4686(02)00682-5.

Martinelli, L., Talvy, S., Liégeois, S., Vanden Berghe, A., Chauveheid, E., Haut, B., 2011. Single-phase flow model development for macroscopic liquid flow evaluation in gas–liquid reactors, by computational fluid dynamics. Chemical Engineering Science 66, 3369–3376. URL: https://linkinghub.elsevier.com/retrieve/pii/S0009250911000418, doi:10.1016/j.ces.2011.01.031.

Moreno Soto, A., 2019. Bubbles on surfaces : diffusive growth and electrolysis. PhD. University of Twente. Enschede, The Netherlands. URL: http://purl.org/utwente/doi/10.3990/1.9789036547246, doi:10.3990/1.9789036547246. iSBN: 9789036547246.

Orvalho, S., Ruzicka, M.C., Olivieri, G., Marzocchella, A., 2015. Bubble coalescence: Effect of bubble approach velocity and liquid viscosity. Chemical Engineering Science 134, 205–216. URL: https://linkinghub.elsevier.com/retrieve/pii/S0009250915003140, doi:10.1016/j.ces.2015.04.053.

Orvalho, S., Stanovsky, P., Ruzicka, M.C., 2021. Bubble coalescence in electrolytes: Effect of bubble approach velocity. Chemical Engineering Journal 406, 125926. URL: https://linkinghub.elsevier.com/retrieve/pii/S1385894720320544, doi:10.1016/j.cej.2020.125926.

Park, H.K., Chung, B.J., 2022. Comparative analysis of bubble behavior between boiling and hydrogen evolving system at horizontal cylinders. Heat and Mass Transfer 58, 779–789. URL: https://link.springer.com/10.1007/s00231-021-03140-8, doi:10.1007/s00231-021-03140-8.

Ribeiro, C.P., Mewes, D., 2006. On the effect of liquid temperature upon bubble coalescence. Chemical Engineering Science 61, 5704–5716. URL: https://linkinghub.elsevier.com/retrieve/pii/S0009250906003034, doi:10.1016/j.ces.2006.04.043.

Rocha, F., Delmelle, R., Georgiadis, C., Proost, J., 2022. Effect of pore size and electrolyte flow rate on the bubble removal efficiency of 3D pure Ni foam electrodes during alkaline water electrolysis. Journal of Environmental Chemical Engineering 10, 107648. URL: https://linkinghub.elsevier.com/retrieve/pii/S2213343722005218, doi:10.1016/j.jece.2022.107648.

Rocha, F., Delmelle, R., Georgiadis, C., Proost, J., 2023. Electrochemical Performance Enhancement of 3D Printed Electrodes Tailored for Enhanced Gas Evacuation during Alkaline Water Electrolysis. Advanced Energy Materials 13, 2203087. URL: https://onlinelibrary.wiley.com/doi/10.1002/aenm.202203087, doi:10.1002/aenm.202203087.

Rodriguez Osuna, I.A., Cobelli, P., Olaiz, N., 2022. Bubble Formation in Pulsed Electric Field Technology May Pose Limitations. Micromachines 13, 1234. URL: https://www.mdpi.com/2072-666X/13/8/1234, doi:10.3390/mi13081234.

Ruiz-Rus, J., Ern, P., Roig, V., Martínez-Bazán, C., 2022. Coalescence of bubbles in a high Reynolds number confined swarm. Journal of Fluid Mechanics 944, A13. URL: https://www.cambridge.org/core/product/identifier/S002211202200492X/type/journal$_a$rticle, doi : 10.1017/jfm.2022.492.$Scott$, $W.T.$, 1968.$AnalyticStudiesofCloudDropletCoalescenceI$.$JournaloftheAtmosphericSciences$25, 54– −65.$URL$: http://journals.ametsoc.org/doi/10.1175/1520-0469(1968)025<0054:ASOCDC>2.0.CO;2, doi : 10.1175/1520 − 0469(1968)025 < 0054 : $ASOCDC$ > 2.0.CO; 2.

Stokes, G.G., 2009. Mathematical and Physical Papers. 1 ed., Cambridge University Press. URL: https://www.cambridge.org/core/product/identifier/9780511702266/type/book, doi:10.1017/CBO9780511702266.

Van Helden, W., Van Der Geld, C., Boot, P., 1995. Forces on bubbles growing and detaching in flow along a vertical wall. International Journal of Heat and Mass Transfer 38, 2075–2088. URL: https://linkinghub.elsevier.com/retrieve/pii/001793109400319Q, doi:10.1016/0017-9310(94)00319-Q.

Vogt, H., 2017. The Quantities Affecting the Bubble Coverage of Gas-Evolving Electrodes. Electrochimica Acta 235, 495–499. URL: https://linkinghub.elsevier.com/retrieve/pii/S0013468617305972, doi:10.1016/j.electacta.2017.03.116.

Yang, X., Baczyzmalski, D., Cierpka, C., Mutschke, G., Eckert, K., 2018. Marangoni convection at electrogenerated hydrogen bubbles. Physical Chemistry Chemical Physics 20, 11542–11548. URL: http://xlink.rsc.org/?DOI=C8CP01050A, doi:10.1039/C8CP01050A.

Yuan, S., Zhao, C., Cai, X., An, L., Shen, S., Yan, X., Zhang, J., 2023. Bubble evolution and transport in PEM water electrolysis: Mechanism, impact, and management. Progress in Energy and Combustion Science 96, 101075. URL: https://linkinghub.elsevier.com/retrieve/pii/S0360128523000059, doi:10.1016/j.pecs.2023.101075.

Zhang, B., Wang, Y., Feng, Y., Zhen, C., Liu, M., Cao, Z., Zhao, Q., Guo, L., 2024. Coalescence and detachment of double bubbles on electrode surface in photoelectrochemical water splitting. Cell Reports Physical Science 5, 101837. URL: https://linkinghub.elsevier.com/retrieve/pii/S2666386424000626, doi:10.1016/j.xcrp.2024.101837.

Zhao, P., Hu, Z., Cheng, P., Huang, R., Gong, S., 2022. Coalescence-Induced Bubble Departure: Effects of Dynamic Contact Angles. Langmuir 38, 10558–10567. URL: https://pubs.acs.org/doi/10.1021/acs.langmuir.2c01404, doi:10.1021/acs.langmuir.2c01404.